Materials Transactions, Vol. 53, No. 1 (2012) pp. 38 to 45
Special Issue on Advanced Materials Science in Bulk Nanostructured Metals

High-Pressure Torsion for Pure Chromium and Niobium

Seungwon Lee[1,2] and Zenji Horita[1,2]

[1]*Department of Materials Science and Engineering, Faculty of Engineering, Kyushu University, Fukuoka 819-0395, Japan*
[2]*WPI, International Institute for Carbon-Neutral Energy Research (I²CNER), Kyushu University, Fukuoka 819-0395, Japan*

Two kinds of body centered cubic (bcc) structure refractory metals, pure Cr and Nb, were subjected to severe plastic deformation through high-pressure torsion (HPT) under applied pressures of 2 and 6 GPa for 2, 3, 4 and 5 revolutions at room temperature. Vickers microhardness is plotted as a function of the distance from the disk center and equivalent strain. It is shown that all hardness values fall on a single curve when they are plotted against equivalent strain for both metals. Vickers microhardness increases with increasing equivalent strain at an early stage of straining and then reaches steady state with the grain size of 200–250 nm in Cr and 240–270 nm in Nb irrespective of the applied pressures. In the steady state, there is no changing in hardness even in applying further straining. Tensile and bending tests show that brittle fracture occurs in Cr but in Nb, the strength significantly increases with some ductility after HPT processing. [doi:10.2320/matertrans.MD201131]

(Received August 24, 2011; Accepted October 31, 2011; Published December 14, 2011)

Keywords: *high-pressure torsion, severe plastic deformation, equivalent strain, bcc metals, ultrafine grains, tensile test, bending test*

1. Introduction

Ultrafine/nano-grained materials have advantages with higher strength and better ductility over their coarse-grained ones. In recent years, much effort has been devoted to develop grain refinement methods and investigating their unusual mechanical properties. Several methods using severe plastic deformation (SPD) have been developed for last 2 decades and typical examples are equal-channel angular pressing (ECAP), high-pressure torsion (HPT) and accumulative roll bonding (ARB).[1,2)]

The fundamental concept of HPT was introduced by Bridgman, where intense shear strain was imparted under high applied pressure.[3)] In the HPT processing, a thin disk is subjected to compression and torsion to produce much larger strain than other SPD methods like ECAP and ARB. It has been demonstrated that HPT is effective to refine the grain size not only of conventional metallic materials but also of hard and brittle materials.[4)] HPT has two advantages over other SPD processes: first, it tends to produce both smaller grain sizes and higher fractions of high-angle grain boundaries and second, it is applicable to hard and brittle materials because application of high pressure prevents cracks from initiation and propagation during processing. It is then anticipated that it can be applicable to hard materials such as refractory metals as investigated in this study.[5–7)]

HPT has been applied to many face-centered cubic (fcc) metals and alloys[8,9)] and also, applied to some hexagonal-closed packed (hcp) metals and alloys.[10–13)] Application of SPD processing to body-centered cubic (bcc) metals and alloys is rather few,[5,14–18)] especially to the metals in Group Va and VIa which have high melting points. It is well known that they are all hard-to-deform metals with higher yield strengths. Although a few reports are available for SPD processing on Cr and Nb,[17,19–21)] they focused on their thermal properties for example, ductile to brittle transition temperature and annealing behavior after SPD processing. This study aims to investigate evolution of microstructures mechanical properties and microstructure on two bcc metals, Cr and Nb after HPT processing.

2. Experimental Materials and Procedures

High purity Cr (99.9%, sintered from powders) and Nb (99.9%, rolled after casting) were received in the form of $10 \times 10 \times 1\,mm^3$ chips and these chips were ground mechanically to a thickness of 0.85 mm. The average grain size was determined using the linear intercept method and they were of 70 μm and 150 μm for Cr and Nb, respectively. These disks were cut with diameter of 10 mm by a wire-cutting electric discharge machine (EDM). The disks were subjected to HPT under a selected pressure of 2 and 6 GPa for 1/4, 2, 3, 4, or 5 revolutions with a rotation speed of 1 rpm at room temperature. The alignment around the rotation axis of the upper and lower axes was adjusted to well within ±0.01 mm for HPT process. Slippage between the disk and the anvils was measured after 1/4 revolutions using the procedure described earlier.[18)]

Vickers microhardness was measured along the 12 radial directions at every 0.5 mm from the disk center to the edge on mechanically polished surface. Averages were taken from twelve measurements at the same distances from the disk center. The disks processed for 4 and 5 revolutions in Cr and 5 revolutions in Nb at each pressure were cut to two halves and polished the cross sectional plane to a mirror-like surface. The hardness measurements were conducted across the thickness on the cross sectional plane at every 0.1 mm from one surface to the other. Each hardness measurement was conducted by using a load of 200 g for a duration time of 15 s.

After processing by HPT, the disks were mechanically polished to a thickness of ~0.50 mm and tensile specimens were cut from the polished disks using the EDM at the 2 mm off-center position as illustrated in Fig. 1(a) with the dimensions of 1.5 mm gauge lengths and 0.7 mm widths. The tensile specimens were pulled to failure at a room temperature using a testing machine operating at a constant rate of cross-head displacement with the initial strain rate of $3.0 \times 10^{-3}\,s^{-1}$.

In this study, bending tests were adopted to evaluate the ductility with inclusion of a compression mode. Bending specimens with dimensions of $0.5 \times 0.5 \times 9\,mm^3$ rod were

cut from the HPT-processed at the position 2 mm from the disk center as illustrated in Fig. 1(b). Three-point bending tests were conducted at room temperature with a cross-head speed of 0.5 mm/s using 8 mm supporting span. Loading was undertaken toward the direction parallel to the pressing direction of the HPT samples. The bending stress σ was measured using the following Euler–Bernoulli beam theory:[22)]

$$\sigma = \frac{3Fl}{2wh^2} \tag{1}$$

where F is the bending load, l is the supporting span (8 mm), w and h are the width and length of the bending specimen (0.5 mm and 0.5 mm), respectively. With bending test, it is possible to apply compression component to sample, then deformation behavior when compression and tension are applied in the same time.

The fracture surfaces after the bending tests were observed using a Hitachi S-4300SE and JEOL JSM-5600 scanning electron microscope (SEM) operating at 20 kV.

Disks with 3 mm diameter were punched out of HPT-processed disks at 3.5 mm from the disk center as illustrated in Figs. 1(a) and 1(b). The TEM samples represent the microstructures at midpoint of thickness.

They were ground to a thickness of 0.15 mm and then thinned using a twin-jet electro-polishing facility in a solution of 5 vol% $HClO_4$ and 95 vol% CH_3COOH at room temperature with an application of 10 V for Cr, and a solution of 4 vol% H_2SO_4 and 96 vol% CH_3OH at 263 K with an application of 20 V for Nb. The microstructures were observed using a Hitachi H-8100 transmission electron microscope (TEM) operating at 200 kV. Selected area electron diffraction (SAED) patterns were taken from regions having diameters of 6.3 μm.

3. Results and Discussions

3.1 Hardness measurement

The average values of Vickers microhardness are plotted in Fig. 2 as a function of the distance from the disk center after HPT processing for $N = 2$, 3, 4 and 5 revolutions under the pressures of 2 and 6 GPa. For both Cr and Nb, Vickers microhardness increases with the distance from the disk center for all numbers of revolutions under both pressures but the hardness saturates to constant levels. In both cases, there is no changing in hardness after reaching the saturation level. However, there is a clear difference between the results of Cr and Nb. First, the hardness level at the saturation is much higher in Cr than in Nb whereas the difference is minor at the as-received condition: Cr = 90 *Hv* and Nb = 75 *Hv*. Second, in the case of Nb, the strain to reach the saturation is smaller than the case of Cr in spite of the same HPT processing condition. These results are similar to Mo and V reported earlier.[5)] The reason for this should be due to the difference in shear modulus. Earlier study showed that when hardness is plotted against equivalent strain divided by shear modulus, a universal plot is attained.[23)] Thus under a given pressure, the sample with larger shear modulus requires more strain to reach a steady state than the sample with smaller shear modulus.

All Vickers microhardness values in Fig. 2 are plotted as a function of the equivalent strain in Fig. 3. Here, the following equation is used for the calculation of the equivalent strain.[18)]

$$\varepsilon = (1 - s) \int_0^N \frac{2\pi r}{\sqrt{3}t(N)}\, dN \tag{2}$$

where r is the distance from the disk center, N is the number of revolutions, s is the fraction of slippage and $t(N)$ is the disk thickness as a function of N during HPT processing. The value of s was measured at each pressure for both metals using a procedure as described earlier[18)] and was found to be in the rage of 0.1 to 0.2. The form of $t(N)$ was determined as a function of N by measuring the thicknesses after several different revolutions as earlier.[9)]

It is apparent that the microhardness data fall on a single curve. Microhardness increases with increasing equivalent strain at an initial stage of straining and saturates to steady-state levels at high strains where the hardness remains unchanged with further straining.

To check homogeneity of the HPT-processed disks, hardness measurement was conducted across the thickness on the cross sectional plane cut along the diameter of each disk. Figure 4 plots hardness against the distance from the disk surface at the disk center and at the distances of 2 and 4 mm located from the disk center. Microhardness is almost constant across the thickness, although the hardness levels become higher with increasing distance from the disk center in consistence with hardness variations shown in Figs. 2 and 3. These results demonstrate that the samples after HPT processing are homogeneously deformed throughout the thickness at any location from the center.

3.2 Transmission electron microscopy

TEM micrographs are summarized in Figs. 5 and 6 including SAED patterns for Cr and Nb after HPT processing, respectively: in each figure, bright-field images on the left and dark-field images on the right. The dark field images were taken with the diffracted beams indicated by arrows in the SAED patterns. The microstructures obtained under 2 GPa are shown in (a) and (b) for 2 and 5 revolutions, respectively, in each of Cr and Nb, and those under 6 GPa are in (c) and (d) for 2 and 4 revolutions, respectively, in Cr and 2 and 5 revolutions, respectively, in Nb. The microstructures were taken from the regions corresponding to the steady-state, which are at 3 mm away from the disk center. The grain size distributions are shown in Figs. 7 and 8 at each HPT conditions in both Cr and Nb, respectively, where (a), (b) is for 2 GPa and (c), (d) for 6 GPa. The average grain sizes and standard deviations are summarized in Table 1. The grain size was obtained from the dark-field images as in Figs. 5 and 6 where the two orthogonal axes of the bright areas were measured for a total of more than 100 grains. With these results, it is found that the average grain size becomes slightly smaller with increasing pressure and increasing number of revolutions. Inspection of the SAED patterns shows also that the misorientation angle of the grain boundary increases with shear straining because the patterns tend to form a net type under 2 GPa for 2 revolutions in both metals as shown in Figs. 5(a) and 6(a). Thus, the micro-

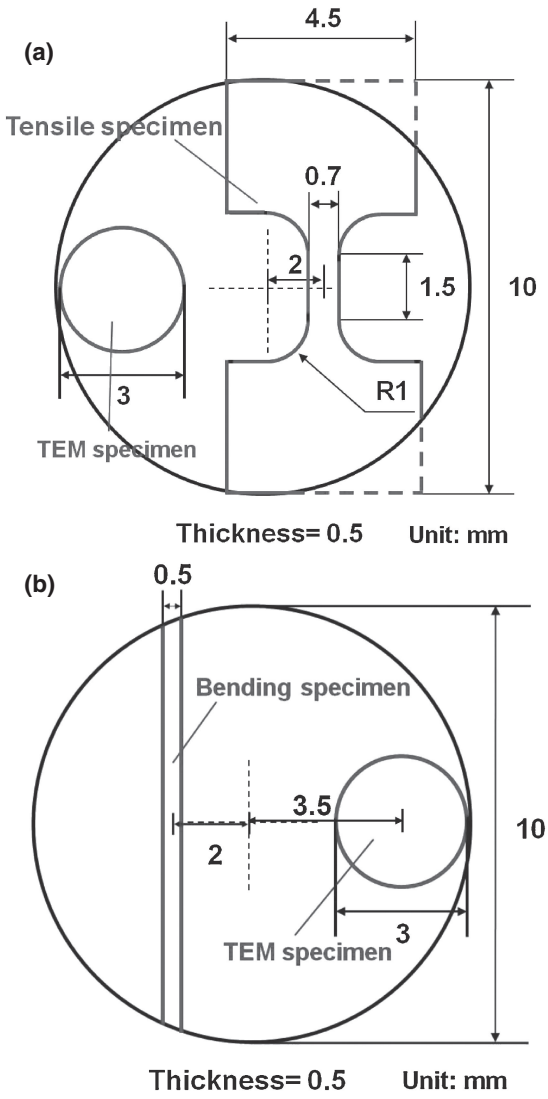

Fig. 1 Dimensions of disk sample including positions for TEM disks and (a) tensile specimen and (b) bending specimen.

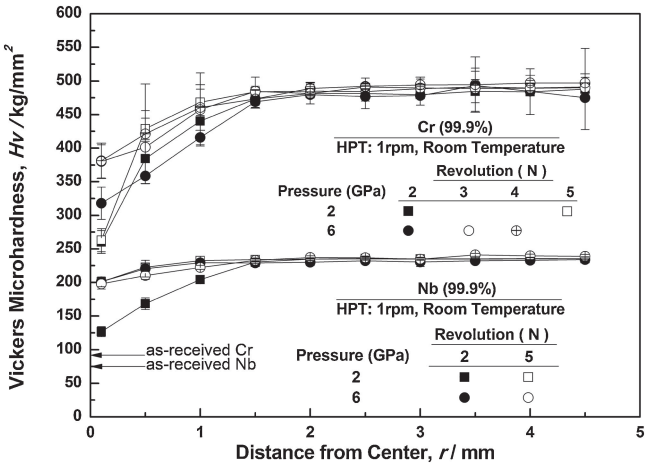

Fig. 2 Vickers microhardness plotted against distance from center for Cr and Nb after HPT processing under 2 and 6 GPa for various revolutions.

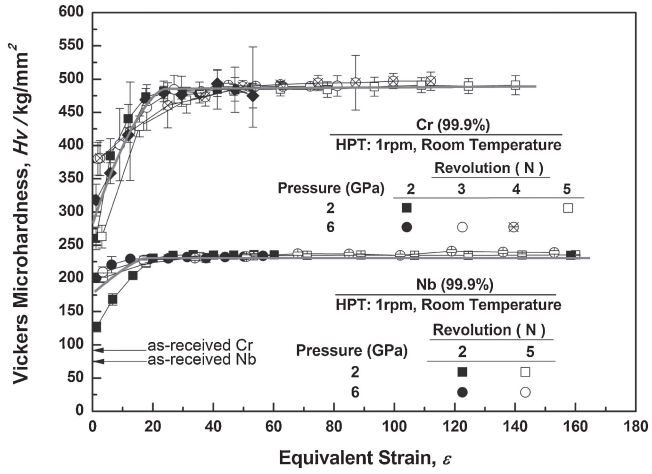

Fig. 3 Vickers microhardness plotted against equivalent strain for Cr and Nb after HPT processing under 2 and 6 GPa for various revolutions.

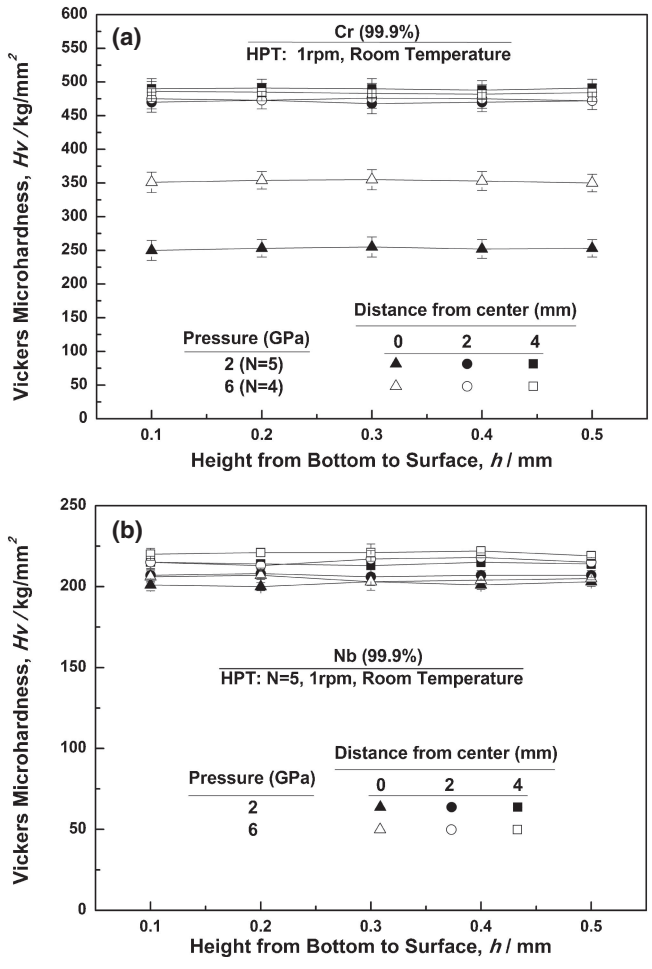

Fig. 4 Vickers microhardness plotted against height from bottom on cross sectional plane for (a) Cr and (b) Nb.

Table 1 Grain sizes for Cr and Nb after HPT process.

Pressure (P)	2 GPa		6 GPa		
Revolution (N)	2	5	2	4	5
Cr	250 nm	210 nm	220 nm	200 nm	—
Nb	270 nm	250 nm	250 nm	—	240 nm

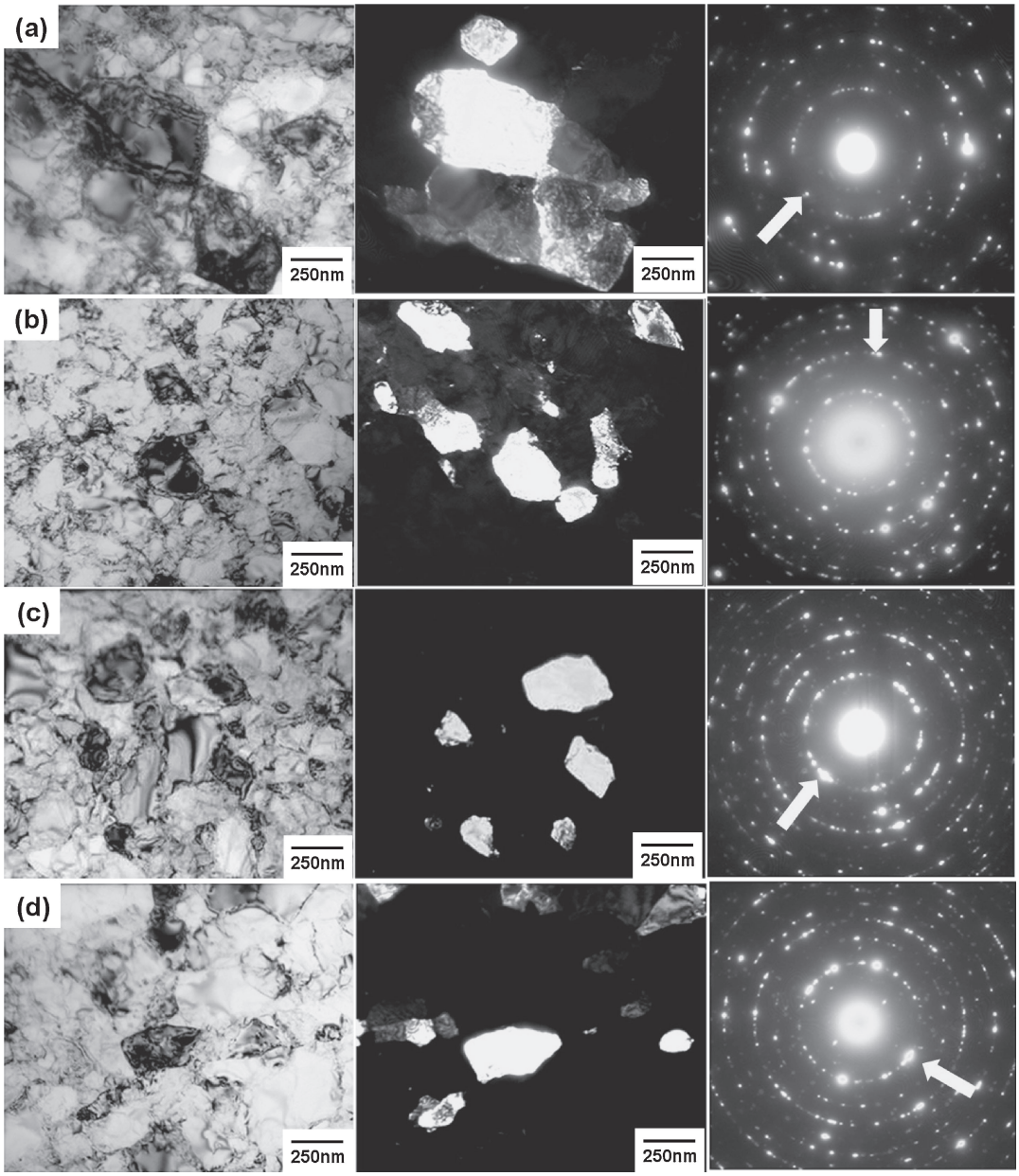

Fig. 5 TEM micrographs and SAED patterns of Cr: under $P = 2$ GPa for (a) 2 revolutions and (b) 5 revolutions, and under $P = 6$ GPa for (c) 2 revolutions and (d) 4 revolutions.

structures after processing by HPT under 2 GPa for 2 revolutions consist of grains with low angle boundaries (subgrains) with the average sizes of ~250 nm in Cr and ~270 nm in Nb. In Figs. 5(b), 5(c), 5(d) and Figs. 6(b), 6(c), 6(d), ring types of SAED patterns form and thus the angles between two neighboring grains becomes high. The grain size decreases to the size of ~200 nm in Cr and ~240 nm in Nb with many dislocations within the grains. The results of the TEM observations are consistent with earlier reports that the microstructure evolves from subgrains with low angle boundaries to grains with high angle boundaries with straining by severe plastic deformation.

3.3 Tensile and bending tests

Stress–strain curves after tensile tests are delineated in Figs. 9(a) and 9(b) for both Cr and Nb, respectively. For Cr, all tensile specimens were failed during loading except the as-received specimen. For Nb, the tensile strength significantly increased to ~1000 MPa with some ductility. The results after bending tests are shown in Figs. 10(a) and 10(b) to delineate nominal stress-displacement curves for Cr and Nb, respectively. Both tensile tests and bending tests are well consistent, where no ductility is present in the HPT-processed Cr but the ductility is appreciable in the HPT-processed Nb. It should be noted that the initial slopes of the stress–strain curves are much smaller than those estimated from the elastic modulus of each metal because of the elastic contribution from the machines. Thus, the ductility was evaluated in this study by subtracting the amount corresponding to the initial slopes of the stress–strain curves. It is concluded that HPT process created excellent bending stresses with good ductility in Nb. Little ductility in Cr can be due to the effect of invisible cracks generated during the HPT process despite application of high pressure.

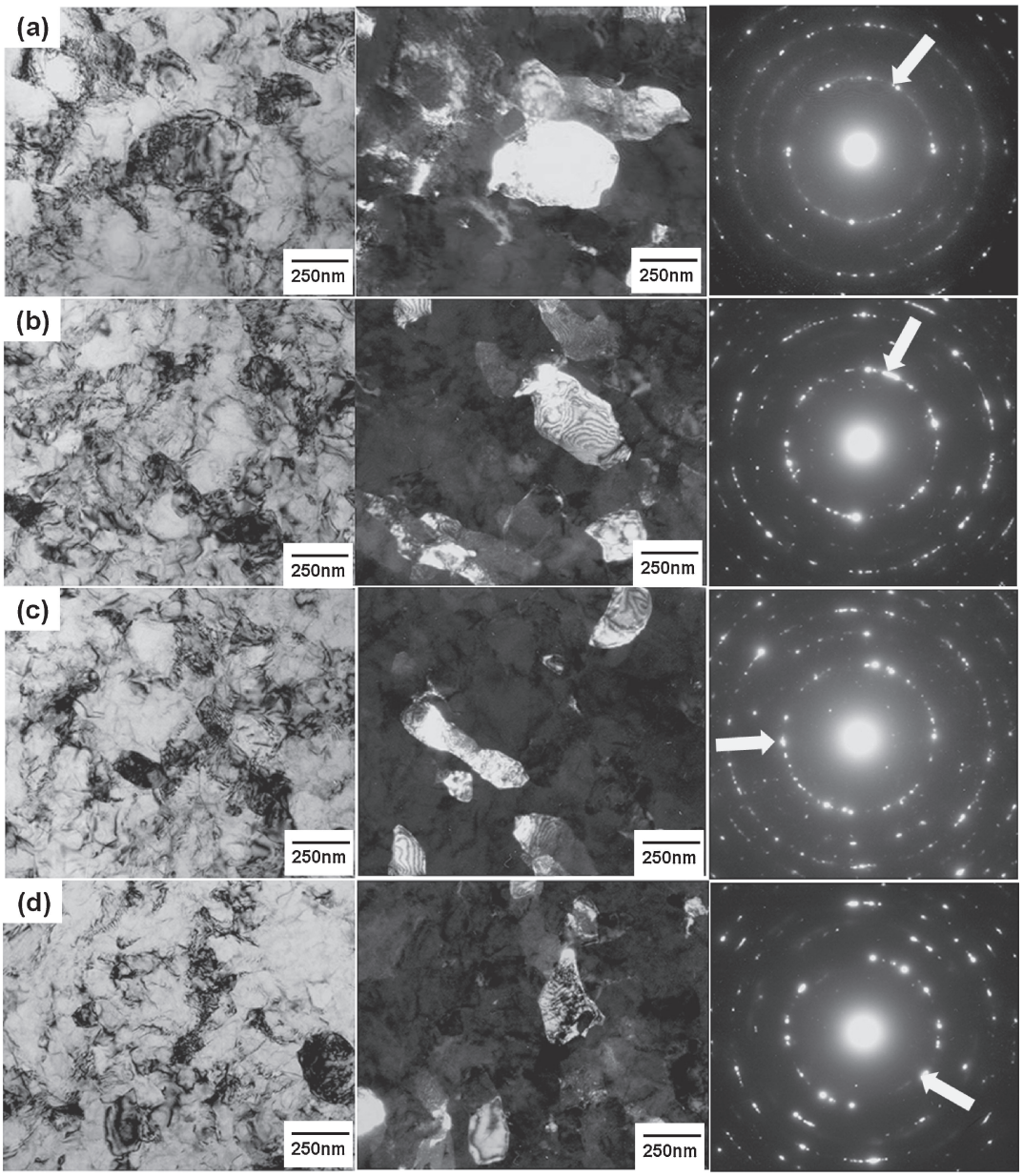

Fig. 6 TEM micrographs and SAED patterns of Nb: under $P = 2$ GPa for (a) 2 revolutions and (b) 5 revolutions, and under $P = 6$ GPa for (c) 2 revolutions and (d) 5 revolutions.

3.4 Fractography

Fractographs after tensile testing are displayed in Figs. 11 and 12 for Cr and Nb, respectively, where (a) represents the as-received sample and (b) and (c) correspond to HPT-processed samples under the pressures of 2 and 6 GPa for the largest number of revolutions. Figure 11 shows a brittle type of fracture in both as-received and HPT-processed specimens. The fracture surfaces of the as-received specimen are rough in the low magnification view but many smooth areas are visible in the high magnification view. For the HPT-processed specimens, the surfaces are smooth with sharp edges on the cross sections in the low magnification view but roughness finely appears on the fractured surfaces as found in the high magnification view. This fine roughness is then considered to be attributed to the fine-grained structure obtained by HPT. By contrast, Fig. 12 shows that the fracture surfaces of Nb are different from those of Cr. All specimens including the as-received specimen exhibit clear reduction in the cross sections as found in the low magnification view. Fine dimples are visible in the high magnification view of the HPT-processed specimens. From the fractography shown in Figs. 11 and 12, it is concluded that the grain refinement does not alter the fracture mode in Cr and Nb although the fractured surfaces reflect the fine grained structures produced by HPT.

4. Summary and Conclusions

(1) Vickers microhardness data fall on a singe curve when plotted as a function of equivalent strain for both Cr and Nb after HPT.

(2) The hardness increases with increasing in the equivalent strain at an early stage of straining and reaches into a steady-state where the microhardness remains unchanged even further straining.

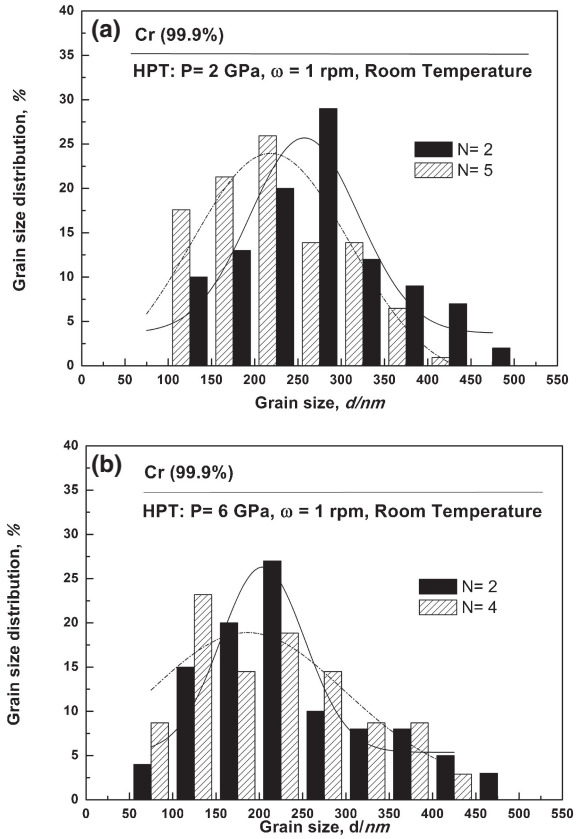

Fig. 7 Grain size distribution of Cr: (a) under $P = 2\,\text{GPa}$ for 2 revolutions and 5 revolutions and (b) under $P = 6\,\text{GPa}$ for 2 revolutions and 4 revolutions.

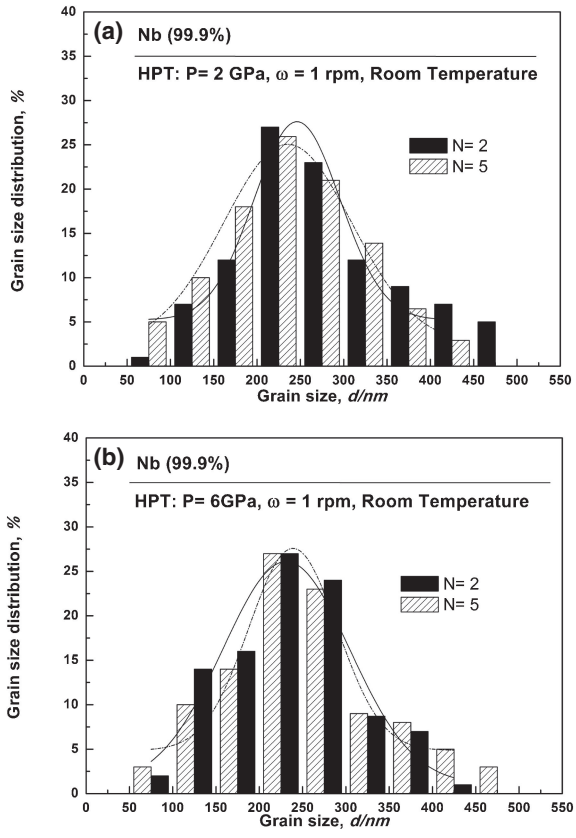

Fig. 8 Grain size distribution of Nb: under (a) $P = 2\,\text{GPa}$ and (b) $P = 6\,\text{GPa}$ for 2 and 5 revolutions.

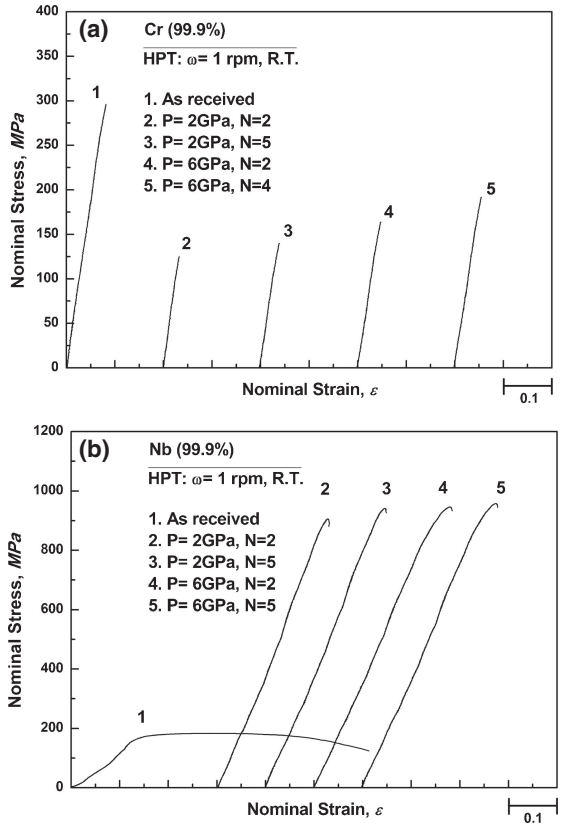

Fig. 9 Nominal stress versus nominal strain curves after tensile testing for (a) Cr and (b) Nb under pressures of 2 and 6 GPa.

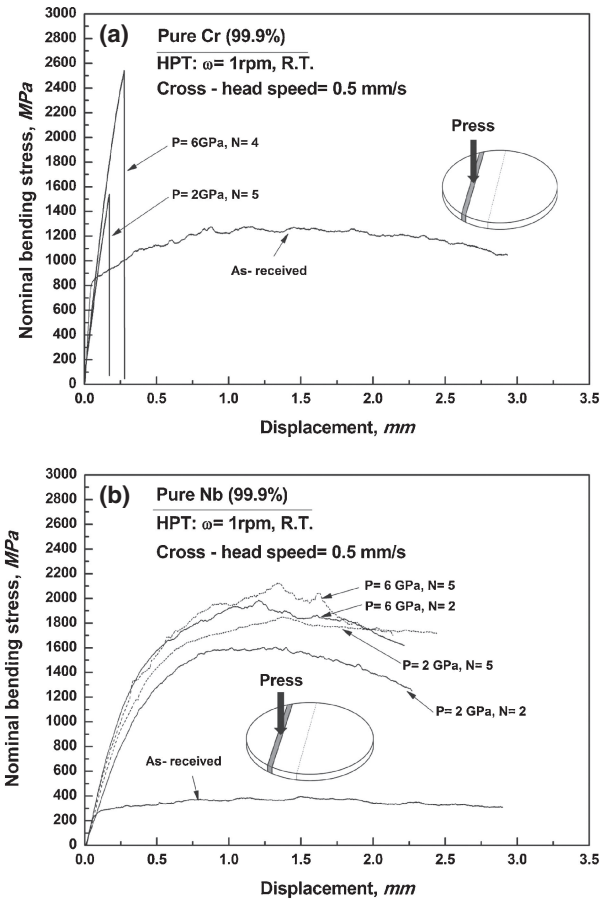

Fig. 10 Nominal bending stress versus displacement curves after bending testing for (a) Cr and (b) Nb under pressures of 2 and 6 GPa.

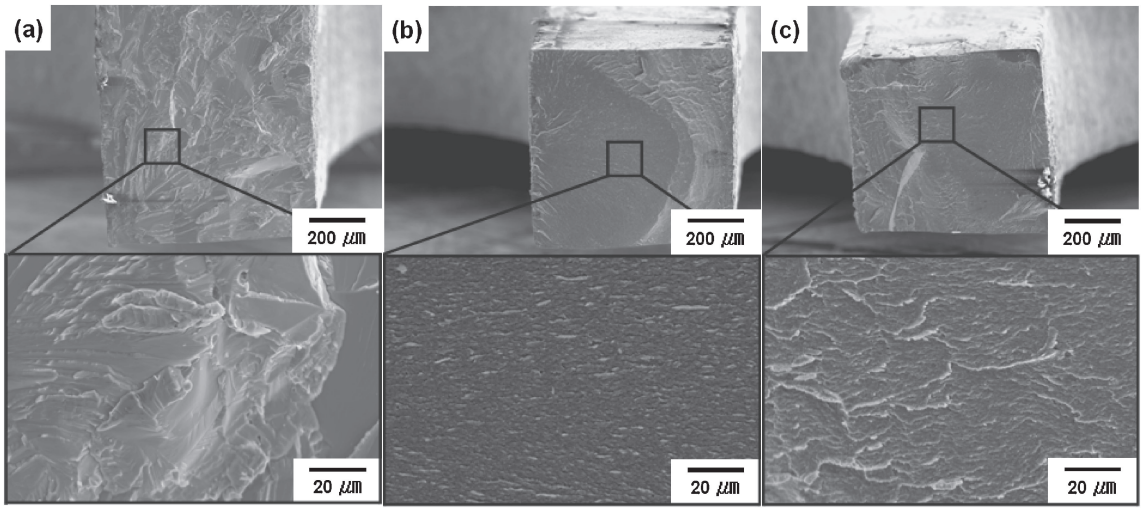

Fig. 11 SEM fractographs after tensile testing for Cr: (a) as-received sample, (b) HPT-processed sample under $P = 2$ GPa for $N = 5$ and (c) HPT-processed sample under $P = 6$ GPa for $N = 4$. Magnified views are shown from selected square areas in overall views.

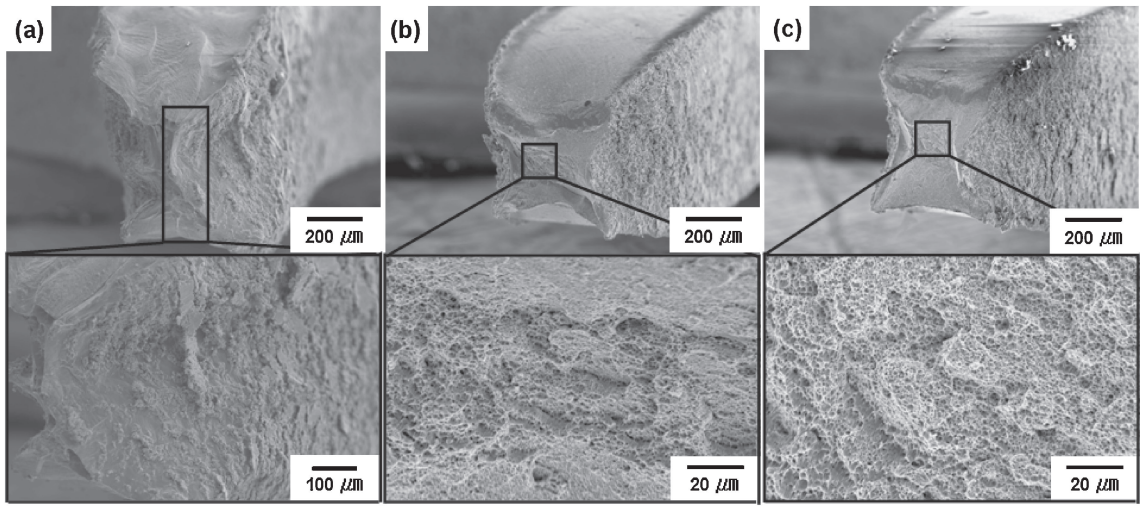

Fig. 12 SEM fractographs after tensile testing for Nb: (a) as-received sample, (b) HPT-processed sample under $P = 2$ GPa for $N = 5$ and (c) HPT-processed sample under $P = 6$ GPa for $N = 5$. Magnified views are shown from selected square areas in overall views.

(3) TEM observation reveals that the grain size is reduced from 70 μm to 200–250 nm in Cr and from 150 μm 240–270 nm in Nb at the saturation level throughout the sample. It is consistent with the tendency of microhardness plotting and grains are arranged along the torsion direction during HPT process.

(4) The tensile test and bending test show that the strength significantly increases with ductility reserved in Nb. Specially, in bending test, Nb shows an excellent ductility with very high strength when compared to as-received Nb.

Acknowledgements

We thank Prof. Kenji Higashida in Kyushu University, for permitting the use of the bending test facility, and Dr. Masaki Tanaka in Kyushu University for careful assistance in using a bending test machine. One of the authors (SL) would like to thank the AQ program for a PhD scholarship. This work was supported in part by a Grant-in-Aid for Scientific Research from the MEXT, Japan, in innovative Areas "Bulk Nanostructured Metals" and in part by Kyushu University Interdisciplinary Programs in Education and Projects in Research Development (P&P).

REFERENCES

1) R. Z. Valiev, R. K. Islamgaliev and I. V. Alexandrov: Prog. Mater. Sci. **45** (2000) 103–189.
2) R. Z. Valiev, Y. Estrin, Z. Horita, T. G. Langdon, M. J. Zehetbauer and Y. T. Zhu: JOM **58** (2006) 33–39.
3) P. W. Bridgman: J. Appl. Phys. **14** (1943) 273–283.
4) G. Sakai, K. Nakamura, Z. Horita and T. G. Langdon: Mater. Sci. Forum **503–504** (2006) 391–396.
5) S. Lee, K. Edalati and Z. Horita: Mater. Trans. **51** (2010) 1072–1079.
6) N. A. Smirnova, V. I. Levit, V. I. Pilyugin, R. I. Kuznetsov, L. S. Davydova and V. A. Sazonova: Fiz. Met. Metalloved. **68** (1986) 1170–1177.
7) T. Hebesberger, H. P. Stuwe, A. Vorhauer, F. Wetscher and R. Pippan: Acta Mater. **53** (2005) 393–402.
8) K. Edalati, T. Fujioka and Z. Horita: Mater. Sci. Eng. A **497** (2008)

168–173.
9) Y. Ito and Z. Horita: Mater. Sci. Eng. A **503** (2009) 32–36.
10) K. Edalati, Z. Horita and Y. Mine: Mater. Sci. Eng. A **527** (2010) 2136–2141.
11) K. Edalati, Z. Horita, S. Yagi and E. Matsubara: Mater. Sci. Eng. A **523** (2009) 277–281.
12) K. Edalati, E. Matsubara and Z. Horita: Metall. Mater. Trans. A **40** (2009) 2079–2086.
13) K. Edalati, A. Yamamoto, Z. Horita and T. Ishihara: Scr. Mater. **64** (2011) 880–883.
14) F. Wetscher, A. Vorhauer and R. Pippan: Mater. Sci. Eng. A **410–411** (2005) 213–216.
15) Y. R. Kolobov, B. Kieback, K. V. Ivanov, T. Weissgaerber, N. V. Girsova, Y. I. Pochivalov, G. Grabovetskaya, M. B. Ivanov, V. U. Kazyhanov and I. V. Alexandrov: Int. J. Refract. Met. Hard Mater. **21** (2003) 69–73.
16) Q. Wei, H. T. Zhang, B. E. Schuster, K. T. Ramesh, R. Z. Valiev, L. J. Kecskes, R. J. Dowding, L. Magness and K. Cho: Acta Mater. **54** (2006) 4079–4089.
17) R. Wadsack, R. Pippan and B. Schedler: Fusion Eng. Des. **66–68** (2003) 265.
18) K. Edalati, T. Fujioka and Z. Horita: Mater. Trans. **50** (2009) 44–50.
19) E. N. Popova, V. V. Popov, E. P. Romanov and V. P. Pilyugin: Phys. Met. Metall. **103** (2007) 407–413.
20) E. N. Popova, V. V. Popov, E. P. Romanov and V. P. Pilyugin: Phys. Met. Metall. **101** (2006) 52–57.
21) V. V. Popov, E. N. Popova, A. V. Stolbovskiy and V. P. Pilyugin: Mater. Sci. Eng. A **528** (2011) 1491–1496.
22) ASTM E290, Standard Test Methods for Bend Testing of Material for Ductility, (ASTM International, West Conshohocken, PA, 2009).
23) K. Edalati and Z. Horita: Mater. Trans. **51** (2010) 1051–1054.